Chemical Engineering Journal 367 (2019) 115–122

Contents lists available at ScienceDirect

Chemical Engineering Journal

journal homepage: www.elsevier.com/locate/cej

Nickel sulfide nanostructures prepared by laser irradiation for efficient electrocatalytic hydrogen evolution reaction and supercapacitors

Tai-Feng Hung[a,b,*], Zu-Wei Yin[a,c], Sophia B. Betzler[a], Wenjing Zheng[a,d], Jiwoong Yang[a], Haimei Zheng[a,e,*]

[a] Materials Sciences Division, Lawrence Berkeley National Laboratory, CA 94720, USA
[b] Energy Storage Technology Division, Green Energy & Environment Research Laboratories, Industrial Technology Research Institute, Hsinchu 31057, Taiwan
[c] College of Energy, Xiamen University, Xiamen 361005, China
[d] Institute of New-Energy Materials, School of Materials Science and Engineering, Tianjin University, Tianjin 300350, China
[e] Department of Materials Science and Engineering, University of California, Berkeley, CA 94720, USA

HIGHLIGHTS

- NiS nanoparticles was synthesized using laser irradiation of an aqueous precursor solution under the ambient condition.
- Crystalline nanoparticles with high phase-purity were achieved without further calcination.
- Other transition metal sulfides were also successfully obtained by this approach.
- Efficient electrocatalytic HER activity and capacitive performances were achieved.

GRAPHICAL ABSTRACT

Nickel sulfide (NiS) nanostructures with great crystallinity and high phase-purity were successfully synthesized using laser irradiation of an aqueous precursor solution under the ambient condition without further calcination. Given the remarkable value of electrochemically active surface area and synergistic effect of Ni^{3+} and Ni^{2+}, the NiS synthesized for 4h delivered not only excellent electrocatalytic activities for hydrogen evolution reaction and but also high specific capacitance and remarkable rate capability for supercapacitors.

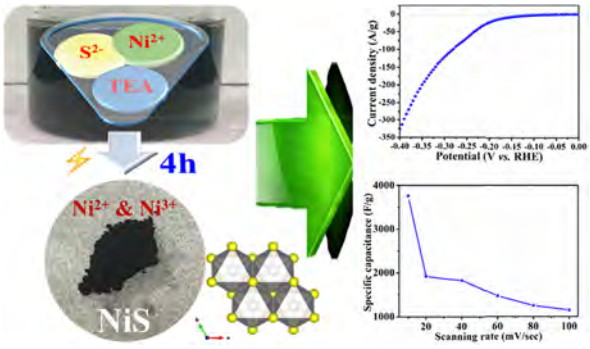

ARTICLE INFO

Keywords:
Transition metal sulfides
Laser irradiation
Hydrogen evolution reaction
Electrochemically active surface area
Supercapacitor

ABSTRACT

Rational design and synthesis of transition metal sulfide complex nanostructures are significant for achieving desired materials properties for a variety of applications. Herein, we synthesized nickel sulfide (NiS) nanostructures using laser irradiation in an aqueous solution and under the ambient condition. Crystalline nanostructures with high phase-purity were achieved without further calcination. Other transition metal sulfides, such as CuS and ZnS, were also successfully synthesized using the laser irradiation approach, suggesting the practical application of this method. The hydrogen evolution reaction (HER) measurements show the NiS nanostructures synthesized for 4h (NiS-4h) not only exhibited competitive overpotential (−159 mV *vs.* RHE at 10 A/g), lower Tafel slope (218 mV/dec) but also delivered long-term stability (14 A/g at −250 mV *vs.* RHE for 12h). Moreover, the NiS-4h functioned as the electrode for supercapacitor with excellent specific capacitance (3761 F/g at 10 mV/s), reversibility and rate capability (1152 F/g at 100 mV/s). These superb electrochemical performances

* Corresponding authors at: Materials Sciences Division, Lawrence Berkeley National Laboratory, CA 94720, USA; Energy Storage Technology Division, Green Energy & Environment Research Laboratories, Industrial Technology Research Institute, Hsinchu 31057, Taiwan (T.-F. Hung).
E-mail addresses: taifeng@itri.org.tw (T.-F. Hung), hmzheng@lbl.gov (H. Zheng).

https://doi.org/10.1016/j.cej.2019.02.136
Received 30 October 2018; Received in revised form 14 February 2019; Accepted 19 February 2019
Available online 20 February 2019
1385-8947/

are attributed to the remarkable value of electrochemically active surface area (ECSA) and synergistic effect of $Ni^{3+}OOH$ for HER electrocatalytic activities, while the co-existence of Ni^{2+} and Ni^{3+} facilitates the rich redox reactions of NiS for supercapacitor.

1. Introduction

Nanostructured transition metal sulfides (TMSs) have drawn growing attention because of their distinct properties in optical, magnetic, electrical, field-emission, photocatalytic, photoelectric, and thermoelectric applications [1]. In recent years, considerable studies give the comprehensive guides on their fundamental mechanisms, progresses and applications of the TMS development [2]. Among these, significant progress has been made on rational design and synthesis of various metal sulfides with controlled shape, composition and structural complexity [2b]. Owing to the merits of high theoretical capacity, suitable potential range and relatively low cost, employing the TMSs as electrode materials for electrochemical energy storage (EES) applications were extensively reported [2b-d,g-k]. Moreover, nanostructured pyrite type materials (*e.g.,* FeS_2, CoS_2, NiS_2, CuS_2) have been reported as efficient electrocatalysts for oxygen evolution reaction (OER), hydrogen evolution reaction (HER), and methanol-tolerant oxygen reduction reaction (ORR) [2e].

To synthesize the nanostructured TMSs, many techniques have been developed, for example, wet-chemistry process [3], anionic exchange process [4], chemical bath deposition [5], hydro/solvothermal reactions [6], thermal sulfurization [7], microwave irradiation [8], atomic layer deposition [9], spray pyrolysis [10], electrodeposition [11], and sonochemical method [12]. In addition to the aforementioned methods, exploiting laser irradiation as an alternative to acquire the nanostructured TMSs was recently reported as a unique one-step process [13]. Depending on the parameters adopted, such as laser wavelength, pulse energy, frequency, *etc.*, the morphology, size and properties of the resulting TMSs vary accordingly [13a,d,e,g,h]. However, this laser irradiation is considered as a facile and environment-friendly technique due to the direct and energy-saving procedures.

In this work, nickel sulfide (NiS) nanostructures were successfully synthesized using laser irradiation of an aqueous precursor solution under the ambient condition without further calcination. Powder X-ray diffractometry (XRD) and transmission electron microscopy (TEM) were utilized to characterize structure and morphology of synthesized NiS compounds. Moreover, this laser irradiation method can also produce copper sulfide (CuS) and zinc sulfide (ZnS) nanostructures with great crystallinity and high phase-purity, demonstrating its general applicability. The HER electrocatalytic activities and specific capacitances of synthesized NiS nanostructures were evaluated in the alkaline medium using linear sweep voltammetry (LSV) and cyclic voltammetry (CV), respectively. This is the first demonstration of utilizing a facile and environmentally friendly laser irradiation to produce NiS nanostructures for HER electrocatalysts and supercapacitors. This approach also offers new possibilities to synthesize a variety of TMSs nanomaterials with extensive applications.

2. Experimental section

2.1. Chemicals

All reagents including Nickel (II) acetate tetrahydrate ($Ni(CH_3COO)_2{\cdot}4H_2O$, 98%, Sigma-Aldrich), Copper (II) acetate ($Cu(CH_3COO)_2$, 98%, Sigma-Aldrich), Zinc (II) acetate dihydrate ($Zn(CH_3COO)_2{\cdot}2H_2O$, ≥99%, Sigma-Aldrich), Thioacetamide (CH_3CSNH_2, ≥99%, Sigma-Aldrich), Triethanolamine ($(HOCH_2CH_2)_3N$, ≥99.5%, Sigma-Aldrich), Ethyl alcohol (C_2H_5OH, ≥99.5%, Sigma-Aldrich), Potassium hydroxide (KOH, 99.99%, Sigma-Aldrich), Carbon black (Super P®, Timcal Ltd.), Platinum on Vulcan Carbon (20 wt% Pt/C, HiSPEC 3000, Fuel Cells Etc) and Nafion® perfluorinated resin solution (5 wt%, Sigma-Aldrich) were used without further purification. Deionized (DI) water produced from a Milli-Q® Integral water purification system (Millipore Ltd.) was used throughout the experiments.

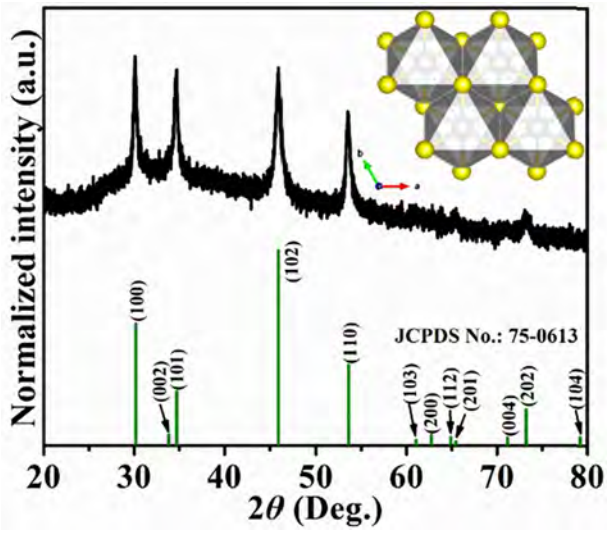

Fig. 1. XRD pattern of NiS-4h, the inset illustrates the corresponding crystal structure.

2.2. Synthesis procedures

To synthesize nickel sulfide (NiS) nanostructures, 10 mmol of CH_3CSNH_2 was firstly well-dissolved in 15 mL of DI water under magnetic stirring. Subsequently, 3 mL of $(HOCH_2CH_2)_3N$ and 4 mmol of $Ni(CH_3COO)_2{\cdot}4H_2O$ were added to the solution, forming a dark green solution at the ambient temperature. Such a precursor solution was subjected to irradiation with an unfocused nanosecond pulsed laser (9.5 mm in diameter, 1064 nm Nd:YAG laser, Continuum Surelite™ III) with the pulse energy of 700 mJ, frequency of 10 Hz, and pulse width of 4–6 ns. During the irradiation, the precursor solution was continuously stirred at 200 rpm to ensure the homogenous reaction. Following centrifugation, repeated rinsing with C_2H_5OH and drying in air (60 °C for 12 h), the synthesized NiS nanostructures were thoroughly ground using pestle and agate mortar to yield fine powders. For convenience, NiS nanostructures synthesized in 2h, 4h, and 6h were hereafter abbreviated as NiS-2h, NiS-4h, and NiS-6h, respectively. As for the copper sulfide (CuS) and zinc sulfide (ZnS) nanostructures, $Cu(CH_3COO)_2$ and $Zn(CH_3COO)_2{\cdot}2H_2O$ were selected as metal sources, whereas the irradiation period was only 2h. The resulting CuS and ZnS nanostructures were collected using the same procedures as described for the NiS nanostructures.

2.3. Material characterizations

The crystallographic properties of synthesized NiS nanostructures were identified by a powder X-ray diffractometer (XRD, D2 PHASER, Bruker AXS Inc.) with a Cu target (λ = 1.541 Å) that was excited at 30 kV and 10 mA. The corresponding PXRD pattern was recorded in the range of 2θ from 20° to 80° at a scanning rate of 0.5 s/step. For morphological observations, the transmission electron micrograph, high-angle annular dark-field scanning transmission electron microscopy (HAADF-STEM) image and energy-dispersive X-ray spectroscopy (EDS) mappings were acquired using a FEI TitanX microscope operated at

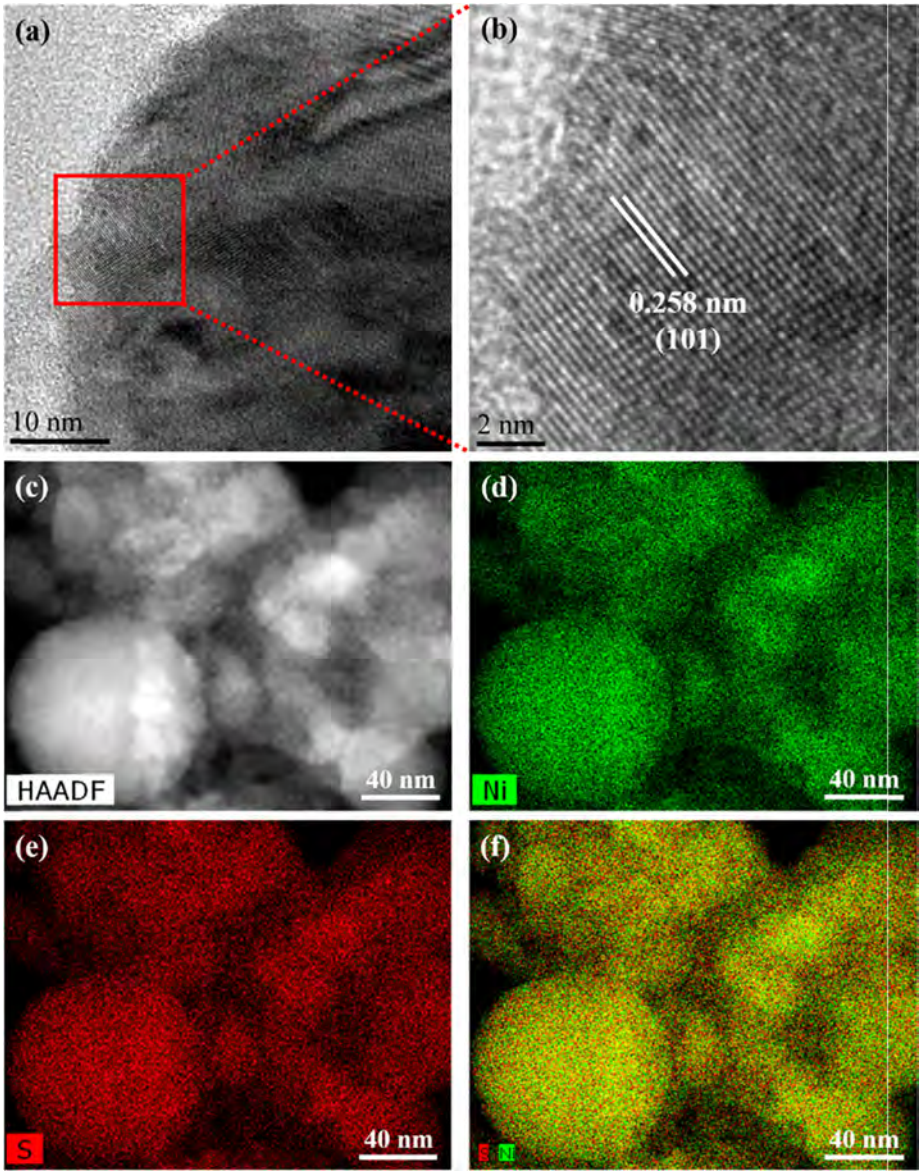

Fig. 2. (a) High-resolution TEM micrograph, (b) lattice fringe, (c) HAADF-STEM image, and (d)-(f) corresponding EDX elemental maps of NiS-4h. Scale bars of (a), (b) and (c)-(f) are 10 nm, 2 nm and 40 nm, respectively.

300 kV, which was equipped with a windowless Bruker EDS detector. The chemical environments were analyzed using X-ray photoelectron spectroscopy (XPS, PHI 5600, PerkinElmer, Inc.) under a monochromatic Al Kα radiation (1486.6 eV) at a spot diameter of 70 μm. The spectra were analyzed using XPSPEAK 4.1 software, in which energy corrections on the high-resolution scans were calibrated by referencing the C 1s peak at 284.6 eV. The Raman spectra were collected using the Horiba Jobin Yvon LabRAM ARAMIS automated scanning confocal Raman microscope equipped with a 532 nm solid-state laser.

2.4. Electrochemical measurements

The electrochemical measurements throughout this study were performed in a standard three-electrode system, which was controlled by an electrochemical analyzer (660E, CH Instruments, Inc.) at ambient temperature. To prepare the working electrode, 8 mg of catalyst (NiS-2h, NiS-4h, NiS-6h and 20 wt% Pt/C) and 2 mg of carbon black were firstly dispersed within the solution (0.5 mL of C_2H_5OH, 0.25 mL of DI water and 0.25 mL of 5 wt% Nafion® solution) by ultrasonication for 30 min. Then, 1 μL of the homogenous suspension was added dropwise onto the surface of a glassy carbon electrode (d = 3 mm, #CHI104, CH Instruments, Inc.), resulting in about 0.113 mg/cm^2 of catalyst loading. A graphite rod and a saturated calomel electrode (SCE, Hg/Hg_2Cl_2 (sat. KCl), #CHI150, CH Instruments, Inc.) served as the counter and reference electrodes, respectively. For hydrogen evolution reaction (HER) catalytic activity test, the linear sweep voltammetry (LSV) and cyclic voltammetry (CV) experiments were conducted in a N_2-saturated 1 M KOH electrolyte. The electrochemical impedance spectroscopy (EIS) measurements in a N_2-saturated 1 M KOH electrolyte were carried out in the same configuration at open circuit potential (OCP) from 100 kHz to 0.01 Hz with an AC potential amplitude of 5 mV to understand the conductivities of synthesized NiS catalysts. The potentials presented in LSV and CV curves were converted against reversible hydrogen electrode (RHE) according to the following equation: $E_{RHE} = E_{SCE} + 0.059\ pH + 0.242$ [7a]. A controlled potential electrolysis was performed at −250 mV *vs.* RHE for 12h, then the generated hydrogen gases (unit: mole and liter) were calculated by considering the amount of accumulated charge. To evaluate the electrochemically active surface area, the double-layer capacitance was measured by CV in the non-faradaic potential region. For capacitive measurement, about 0.566 mg/cm^2 of active materials were loaded onto the working electrode.

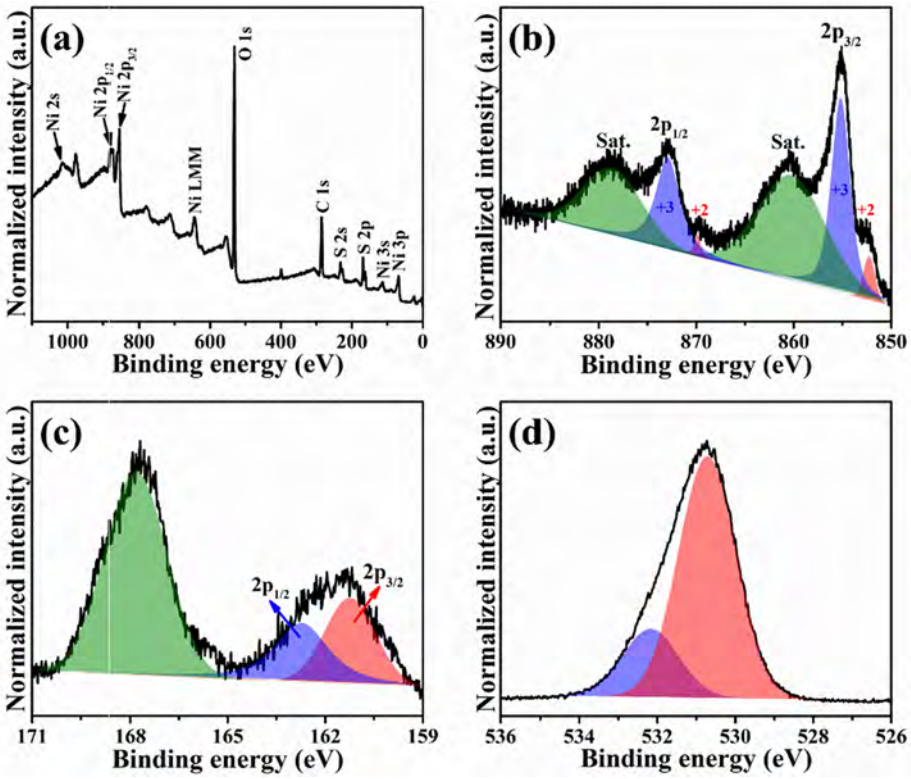

Fig. 3. XPS analysis of NiS-4h: (a) Full-range survey and high-resolution (b) Ni 2p, (c) S 2p, and (d) O 1s spectra. The green, blue and red peaks in (b) are the shark-up satellites, Ni^{3+} and Ni^{2+} signals, respectively. The green, blue and red peaks of (c) represent the sulfate, S $2p_{1/2}$ and S $2p_{3/2}$ peaks. The blue and red peaks in (d) correspond to the $Ni^{3+}OOH$ and $Ni^{2+}SO_4$. (For interpretation of the references to colour in this figure legend, the reader is referred to the web version of this article.)

The CV tests were carried out in a N_2-saturated 6 M KOH electrolyte from the potential range between 0 and 0.55 V *vs.* SCE and different scanning rates to estimate the capacitive performances. The corresponding specific capacitance (C_s, F/g) can be calculated from the CV curves using the Eq. (1) [14]:

$$C_s = \int idv/2(V_s \times \Delta v \times m) \quad (1)$$

where $\int idv$ is the area under the CV curve in the testing potential range; V_s (mV/s) is the scanning rate; Δv (V) is the testing potential range; m (g) is the mass of the active materials on the surface of glassy carbon.

3. Results and discussion

Fig. 1 plots the XRD pattern of the synthesized NiS-4h recorded in the range of 2θ from 20° to 80° to identify its crystallographic structure and phase purity. There are well-defined diffraction peaks at 2θ = 30.2°, 33.8°, 34.7°, 45.9°, 53.6°, 61.1°, 62.7°, 64.9°, 65.4°, 71.2°, 73.2° and 79.2°, which can be assigned to the (1 0 0), (0 0 2), (1 0 1), (1 0 2), (1 1 0), (1 0 3), (2 0 0), (0 0 4), (2 0 2) and (1 0 4) planes of hexagonal α-NiS (JCPDS No.: 75–0613, space group: P63/mmc, a = b = 3.42 Å, c = 5.30 Å, inset of Fig. 1a shows the crystal structure) [6m,7a]. No additional peaks are detected, showing high purity of the synthesized NiS-4h.

Fig. 2 shows TEM characterization of the structure and morphology of NiS-4h. The lattice fringes in the high-resolution TEM images are well-resolved, which can be indexed to the (1 0 1) plane of hexagonal α-NiS (Fig. 2b) [7a]. The resulting NiS-4h with spherical morphology is clearly revealed from the high-angle annular dark-field scanning TEM (HAADF-STEM) micrograph in Fig. 2c, which was appeared as aggregated particles with diameters of the most in the range of 40–60 nm. The corresponding EDX elemental maps (Fig. 2d–f) display the uniform distribution of Ni and S throughout the NiS nanostructures. Although significant aggregation and large size distribution of the nanostructures are observed, the sample shows the great crystallinity and high phase-purity.

To collect detailed information on the chemical environments of the NiS-4h sample, we conducted X-ray photoelectron spectroscopy (XPS) analysis and the corresponding spectra are illustrated in Fig. 3. The full-range survey spectrum (Fig. 3a) shows the peaks assigned to Ni 2p and S 2p. The C 1s and O 1s signals are also observed, which can be attributed to the NiS exposure to air [6f]. Fig. 3b–d present the high-resolution Ni 2p, S 2p and O 1s spectra analyzed using the Gaussian-Lorentzian fitting method. Ni 2p spectrum (Fig. 3b) is composed of two spin–orbit doublets ($2p_{1/2}$ and $2p_{3/2}$) and two shark-up satellites (green peaks) [6g-i,8b]. The binding energies of 852.3 eV and 869.9 eV corresponded to the Ni^{2+} (red peaks) and those at 855.2 eV and 872.9 eV were the characteristic of Ni^{3+} (blue peaks), which were close to the previously reported value for NiS [6f-i,8b]. These results showed that nickel presents in two valence states, providing rich redox reactions of NiS [6i]. For S 2p spectrum (Fig. 3c), the constitute peak at the binding energy of 161.2 eV (red) is assigned to S^{2-} and the peak at 162.7 eV (blue) could be owed by the sulfur ion in low coordination at NiS surface [6f,6i,8b]. The peak at 167.8 eV (green) is likely due to sulfate resulting from surface oxidation [4a,6f,6i]. For O 1s spectrum (Fig. 3d), the composed peaks at the binding energies of 530.7 eV and 532.2 eV are associated with the $Ni^{3+}OOH$ and $Ni^{2+}SO_4$ [15], which are consistent with the results obtained from Ni 2p and S 2p spectra. Therefore, the above results confirmed that the surface of NiS-4h composed of Ni^{2+}, Ni^{3+} and S^{2-}.

We further explore the influence of reaction time on the crystal structures and morphologies of the resulting NiS samples. The XRD patterns and TEM micrographs of NiS-2h and NiS-6h are shown in Fig. S1. It is evident that the XRD patterns of NiS-2h (Fig. S1a) and NiS-6h (Fig. S1c) match well with hexagonal α-NiS of NiS-4h (Fig. 1). This indicates that the crystalline structure and phase purity of the resulting NiS compounds are not affected with the increase of laser irradiation. However, there are distinct changes in the particle sizes and morphology. More uniform nanostructures with the average diameters of 20–30 nm are obtained from the NiS-2h (Fig. S1b). With increasing the reaction time, the particles become larger. Some large particle of 60–80 nm are observed for NiS-6h (Fig. S1d). We propose a general growth mechanism for the formation of NiS nanostructures as the following. First, the Ni^{2+} ions were chelated by the $(HOCH_2CH_2)_3N$, forming the $Ni[(HOCH_2CH_2)_3N]^{2+}$ complexes (Eq. (2)). With the temperature rise during the laser irradiation, Ni^{2+} ions can be released

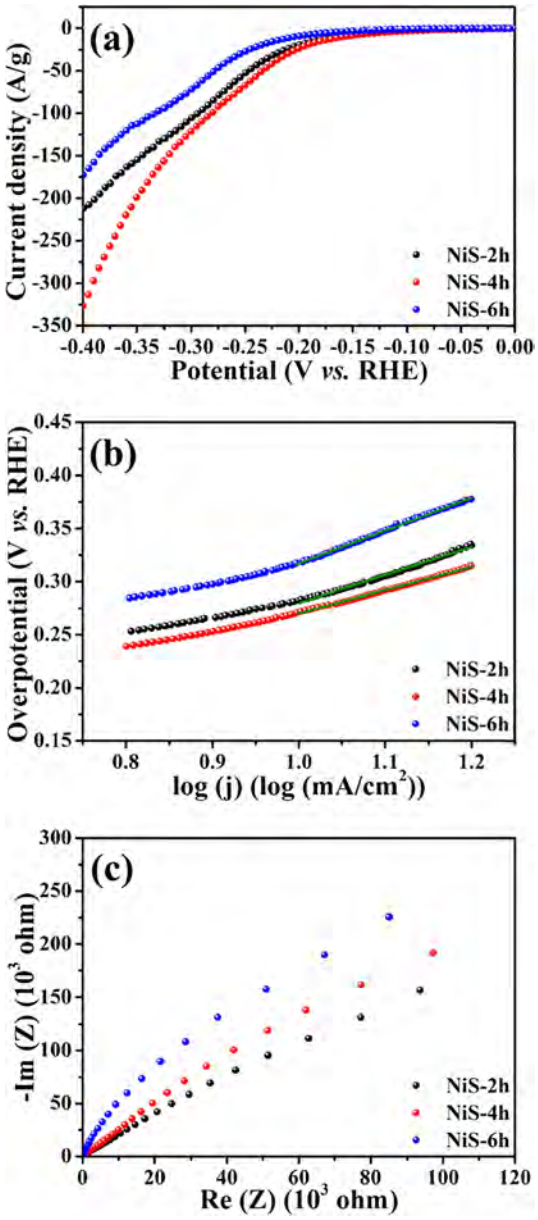

Fig. 4. (a) Linear sweep voltammograms, (b) Tafel plots and (c) electrochemical impedance spectra of NiS-2h (•), NiS-4h (•) and NiS-6h (•) collected in a N_2-saturated 1 M KOH electrolyte.

from the $Ni[(HOCH_2CH_2)_3N]^{2+}$ complexes and sequentially react with the CH_3CSNH_2, leading to the formation of NiS (Eq. (3)). Similar reaction mechanisms are described for synthesizing the SnS nanocrystals and films in the presence of $(HOCH_2CH_2)_3N$ [16]. The NiS nanostructures grow and go through Ostwald Ripening during further laser irradiation.

$$Ni^{2+} + (HOCH_2CH_2)_3\ N \rightarrow Ni[(HOCH_2CH_2)_3N]^{2+} \quad (2)$$

$$Ni[(HOCH_2CH_2)_3N]^{2+} + CH_3CSNH_2 + 2OH^- \rightarrow NiS + CH_3CONH_2 + (HOCH_2CH_2)_3\ N + H_2O \quad (3)$$

To further investigate the applicability of laser irradiation method for synthesis of other transition metal sulfides, we conducted the additional experiments using copper and zinc precursors. XRD patterns of the products synthesized from the copper and zinc sources reveal hexagonal copper sulfide (CuS, Fig. S2a, JCPDS No.: 78–2121, space group: P63/mmc, a = b = 3.79 Å, c = 16.34 Å) and cubic zinc sulfide (ZnS, Fig. S2b, JCPDS No.: 77–2100, space group: F-43 m, a = b = c = 5.42 Å) structures. In addition, the particle sizes of CuS nanostructures are 30 nm and ZnS nanostructures are 5 nm (Fig. S3a and c). High-resolution TEM micrographs show both are highly crystalline (Fig. S3b and d). Those results demonstrate that the laser irradiation method can be used to synthesize a variety of transition metal sulfides. It is reasonable to speculate that their formation mechanisms would also be the same as those discussed for the NiS.

The HER electrocatalytic activities of synthesized NiS were evaluated using linear sweep voltammetry (LSV) in N_2-saturated 1 M KOH electrolyte. Fig. 4a compares the LSV curves of NiS-2h, NiS-4h and NiS-6h in the potential range of 0 to −0.4 V *vs.* RHE at a scan rate of 2 mV/s. It is obvious that NiS-4h exhibited the smallest onset potential (−34 mV *vs.* RHE at −1 A/g) and reached a current density of 10 A/g at an overpotential (η) of −159 mV *vs.* RHE. The HER activities of NiS-2h and NiS-6h followed that of NiS-4h, achieving 10 A/g at the η values of −165 mV and −204 mV *vs.* RHE, respectively. The corresponding Tafel plots (Fig. 4b) fitted to the Tafel equation ($\eta = b\log j + a$, where j is the current density and b is the Tafel slope) reveal that the Tafel slopes of NiS-2h, NiS-4h and NiS-6h were about 266, 218 and 310 mV per decade, respectively. Fig. S4 plots the HER activity of commercial 20 wt% Pt/C measured using the same procedures as that for NiS samples. The current density recorded at −200 mV *vs.* RHE is 654 A/g and the Tafel plot of Pt/C is 90 mV per decade. Although the HER activity of NiS-4h (24 A/g @ −200 mV *vs.* RHE and 218 mV per decade) is not superior to that of Pt/C, NiS is attractive as HER catalyst as it is cost effective by replacing the noble metal. To understand the conductivities of synthesized NiS catalysts, the electrochemical impedance spectroscopy (EIS) measurements in a N_2-saturated 1 M KOH electrolyte were carried out at open circuit potential (OCP) from 100 kHz to 0.01 Hz with an AC potential amplitude of 5 mV. As shown in Fig. 4c, each Nyquist plot starts at a resistance of 10–20 ohm, which is ascribed to the internal resistance of the strongly alkaline electrolyte [6c]. Moreover, there is almost no charge-transfer resistance (R_{ct}) observed from synthesized NiS catalysts, indicating their high internal conductivities. These results are consistent with those of the nanoporous transition metal sulfides (M = Fe, Co, Ni and Mn) film-modified GC electrode measured in 1 M NaOH medium [11b]. In addition to the electrocatalytic onset and Tafel slope, another vital factor to evaluate an electrocatalyst is its stability under long-term testing. Fig. S5 shows a controlled potential electrocatalysis of NiS-4h at −250 mV *vs.* RHE in N_2-saturated 1 M KOH electrolyte. As indicated, NiS-4h delivered a stable cathodic current density of about 14 A/g over 12h, showing the remarkable long-term HER stability. According to the linear charge accumulation *versus* time (inset of Fig. S5), the accumulated charge of NiS-4h for 12h is about 6.73 C, meaning that approximately 4.4 mol and 97.7 L of hydrogen were produced per gram of NiS-4h, respectively.

For better understanding of their HER performance trend and intrinsic activities, the electrochemically active surface area (ECSA) of the catalyst should be evaluated since ESCA is well known to significantly impact the electrocatalytic performance of a catalyst [3c,6c,6k,6l]. A widely adopted technique is to calculate the relative ECSA based on the measurement of double-layer capacitance (C_{dl}) in the non-faradaic potential region [17]. It is generally accepted that the C_{dl} is linearly proportional to ECSA. The C_{dl} of a catalyst can be conveniently deduced from cyclic voltammetry (CV) measurements at various scan rates. Fig. 5a–c show the cyclic voltammograms of NiS-2h, NiS-4h and NiS-6h measured in the range of 0.11 to 0.21 V *vs.* RHE at different scan rates. Plotting the halves of the anodic and cathodic current density difference at the center of the potential range *versus* the scan rate resulted in a linear relationship for each catalyst, as shown in Fig. 5d. The C_{dl} values obtained by linear fitting those plots were 3.59, 3.76 and 2.97 mF/cm^2 for NiS-2h, NiS-4h and NiS-6h. Assuming the C_{dl} value to be 40 μF/cm^2 for a smooth electrode [18], the roughness factor (RF) values of these NiS samples were calculated to be 89.8 (NiS-2h), 94.0 (NiS-4h) and 74.3 (NiS-6h). Accordingly, the ECSA values calculated as the ratio between RF and geometrical area [19] are 6.3, 6.6 and 5.2 cm^2 for NiS-

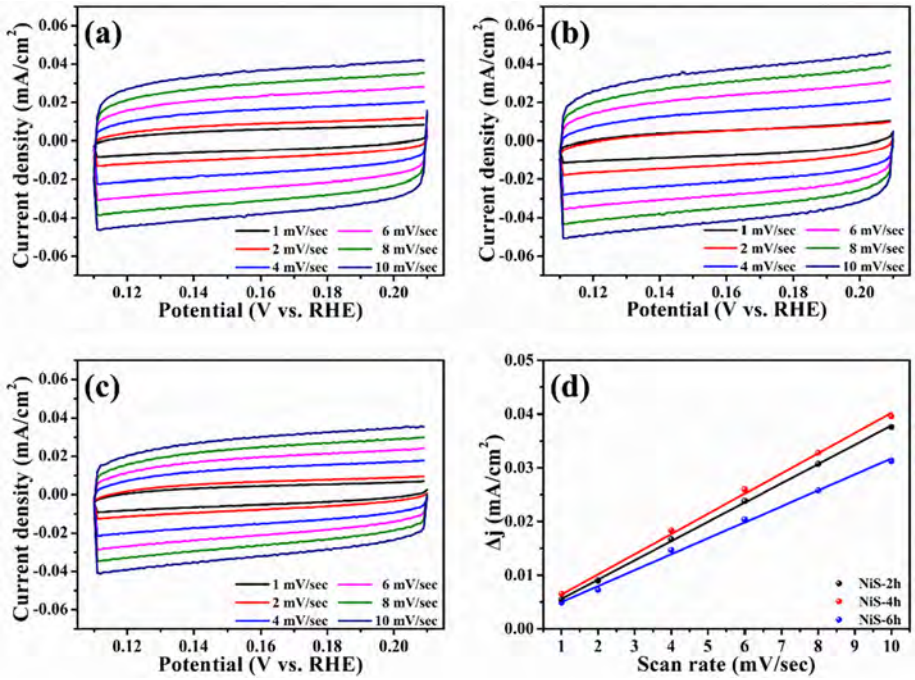

Fig. 5. Cyclic voltammograms of (a) NiS-2h, (b) NiS-4h and (c) NiS-6h recorded in 0.11–0.21 V *vs.* RHE at scan rates from 1 to 10 mV/s in N_2-saturated 1 M KOH electrolyte. (d) Scan rate dependence of the current densities of NiS-2h (•), NiS-4h (•) and NiS-6h (•) at 0.16 V *vs.* RHE and their corresponding linear fittings (solid lines).

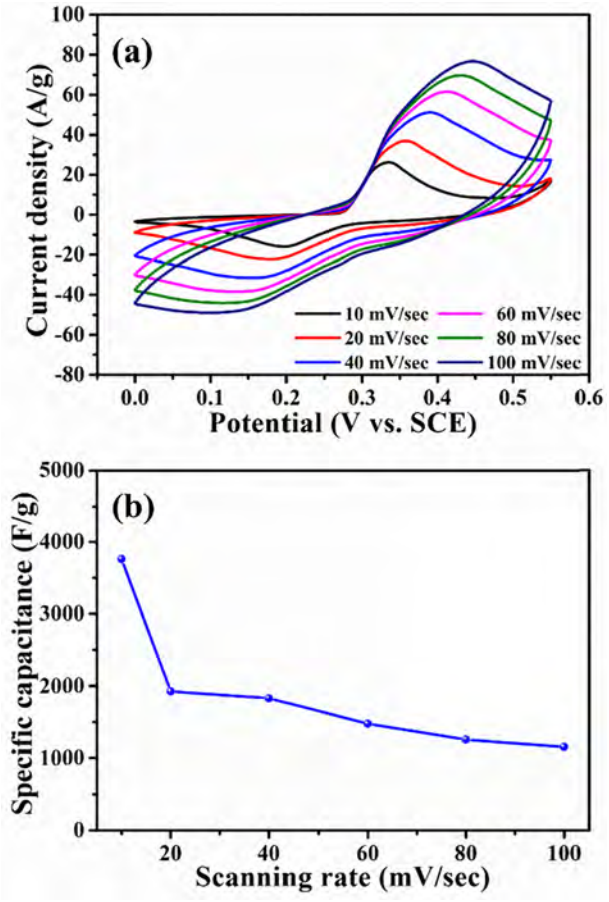

Fig. 6. (a) Cyclic voltammograms and (b) average specific capacitances of NiS-4h recorded in 0–0.55 V *vs.* SCE at scan rates from 10 to 100 mV/s in N_2-saturated 6 M KOH electrolyte.

2h, NiS-4h and NiS-6h.

Recently, Wang et al. reported that amorphous $Ni^{3+}OOH$ electrodeposited on the Ni_3S_2@nickel foam exhibited synergistic effect for improving its electrocatalytic HER activity in 1 M NaOH electrolyte [20]. The Raman spectra of NiS compounds synthesized by 2h, 4h and 6h (Fig. S6) revealed that the main peak was centered at around 490 cm^{-1}, which could be associated with the β-$Ni^{3+}OOH$ [21]. This is consistent with the results obtained from the XPS analysis (Fig. 3b and d), approving that the Ni^{3+} was contributed by the NiOOH. Moreover, the quantitative analysis of Ni^{3+} presented in the synthesized NiS compounds was compared in Table S1, where the results were adopted from the high-resolution Ni 2p spectra in Fig. 3b and Fig. S7. As listed, the sum of integrated area acquired from the Ni^{3+} peaks increased in the order of NiS-4h > NiS-2h > NiS-6h. Consequently, the NiS-4h with such high ECSA value and Ni^{3+} proportion undoubtedly contribute to its excellent HER catalytic activities as shown in Fig. 4a and b.

Except for the HER electrocatalysts, intensive studies have also focused on supercapacitors using NiS as electrode materials in an alkaline solution in the recent years. Fig. 6a depicts the CV curves of NiS-4h measured by three-electrode configuration in N_2-saturated 6 M KOH electrolyte at scan rates varying 10 to 100 mV/s to estimate its electrochemical performance used for supercapacitor. It is apparent that a couple of well-defined redox peaks in each CV curve were observed in a potential range of 0–0.55 V *vs.* SCE. The shape of CV curves is distinguishable from the rectangular shape for electric double-layer capacitors, indicating that the energy storage of NiS electrode is mainly attributed to the pseudocapacitive behavior based on the reversible oxidation of NiS to NiSOH (charge) and reduction of NiSOH to NiS (discharge) as revealed in Eq. (4) [4a,6f-h,6n,14a].

$$NiS + OH^- \leftrightarrow NiSOH + e^- \quad (4)$$

It is well-known that the capacitance of pseudocapacitors in an alkaline solution is mainly derived from the combination of electric double-layer charge storage at the electrode-electrolyte interface, the surface redox reaction of the active material and the hydroxyl ion diffusion [22]. Further increasing the scan rate causes a shift of the anodic and cathodic peaks to higher (oxidation reaction) and lower (reduction reduction) potentials, which indicates that the charge transfer kinetics are the limiting step. Furthermore, a linear relationship between peak current and square root of scan rate is observed (Fig. S8), confirming that the electrode reaction was a diffusion-controlled process [4a,23]. Fig. 6b plots the average specific capacitance, calculated by integrating each CV curve, as a function of the scan rate. It can be seen that the

specific capacitance obtained at 10 mV/s was as high as 3761 F/g. This value was about 7.8 times higher than that of the NiS nanosheets [6n] and comparable with the results listed in Table S2. Even the scan rate increases to 100 mV/s, more importantly, the specific capacitance was about 60% of the value recorded from 20 mV/s, reflecting the good rate capability. Such outstanding electrochemical performances can be attributed to the co-existence of Ni^{2+} and Ni^{3+} in the NiS as verified by XPS analysis, enabling the rich redox reactions [6i].

4. Conclusions

In summary, this study presents a facile and environmentally friendly approach to synthesis of various transition metal sulfides (NiS, CuS and ZnS) by laser irradiation of an aqueous precursor solution under the ambient condition. The resulting products show great crystallinity and high phase-purity without further calcination. Taking NiS as an example, with increasing the duration of laser irradiation from 2h to 6h, the crystalline structure and phase purity of resulting NiS compounds were not affected while the particle sizes increased from 20–30 nm to 60–80 nm. Given by the remarkable ECSA value and synergistic effect of Ni^{3+}OOH, the NiS-4h with particle size of 40–60 nm delivered the considerable HER electrocatalytic activity in an alkaline medium including comparable overpotential (-159 mV *vs.* RHE at 10 A/g), lower Tafel slope (218 mV/dec) and long-term stability (14 A/g at −250 mV *vs.* RHE for 12h). In addition to the fascinating HER performances, the NiS-4h used as electrode material for supercapacitor also possessed the outstanding specific capacitance (3761 F/g at 10 mV/s), reversibility and rate capability (1152 F/g at 100 mV/s). Such favorable electrochemical characteristics of the synthesized NiS can be attributed to the co-existence of Ni^{2+} and Ni^{3+} enabling the rich redox reactions of NiS.

Conflicts of interest

The authors declare no competing financial interests.

Acknowledgements

This work was funded by U.S. Department of Energy (DOE), Office of Science, Office of Basic Energy Sciences (BES), Materials Sciences and Engineering Division under Contract No. DE-AC02-05-CH11231 within the KC22ZH program. Work at the Molecular Foundry was supported by the Office of Science, Office of Basic Energy Sciences, of the U.S. Department of Energy under Contract No. DE-AC02-05CH11231. T.F.H. was funded by the Bureau of Energy (BOE), Ministry of Economic Affairs (MOEA), Taiwan. Z.W.Y. and S.B.B. acknowledge financial supports from China Scholarship Council (201606310151) and Alexander von Humboldt Foundation, respectively.

Appendix A. Supplementary data

Supplementary data to this article can be found online at https://doi.org/10.1016/j.cej.2019.02.136.

References

[1] (a) C.H. Lai, M.Y. Lu, L.J. Chen, Metal sulfide nanostructures: synthesis, properties and applications in energy conversion and storage, J. Mater. Chem. 22 (2012) 19–30;
(b) L. Shen, L. Yu, H.B. Wu, X.Y. Yu, X. Zhang, X.W. Lou, Formation of nickel cobalt sulfide ball-in-ball hollow spheres with enhanced electrochemical pseudocapacitive properties, Nature Commun. 6 (2015) 6694;
(c) S. Xiao, X. Li, W. Sun, B. Guan, Y. Wang, General and facile synthesis of metal sulfide nanostructures: In situ microwave synthesis and application as binder-free cathode for Li-ion batteries, Chem. Eng. J. 306 (2016) 251–259.

[2] (a) Z.H. Ge, L.D. Zhao, D. Wu, X. Liu, B.P. Zhang, J.F. Li, J. He, J. Low-cost, abundant binary sulfides as promising thermoelectric materials, Mater. Today 19 (2016) 227–239;
(b) X.Y. Yu, L. Yu, X.W. Lou, Metal sulfide hollow nanostructures for electrochemical energy storage, Adv. Energy Mater. 6 (2016) 1501333;
(c) X. Han, X. Wu, C. Zhong, Y. Deng, N. Zhao, W. Hu, NiCo2S4 nanocrystals anchored on nitrogen-doped carbon nanotubes as a highly efficient bifunctional electrocatalyst for rechargeable zinc-air batteries, Nano Energy 31 (2017) 541–550;
(d) Y. Xiao, J.Y. Hwang, I. Belharouak, Y.K. Sun, Superior Li/Na-storage capability of a carbon-free hierarchical CoSx hollow nanostructure, Nano Energy 32 (2017) 320–380;
(e) M.R. Gao, Y.R. Zheng, J. Jiang, S.H. Yu, Pyrite-type nanomaterials for advanced electrocatalysis, Acc. Chem. Res. 50 (2017) 2194–2204;
(f) A. Eftekhari, Electrocatalysts for hydrogen evolution reaction, Int. J. Hydrogen Energy 42 (2017) 11053–11077;
(g) W. Kang, Y. Wang, J. Xu, Recent progress in layered metal dichalcogenide nanostructures as electrodes for high-performance sodium-ion batteries, J. Mater. Chem. A 5 (2017) 7667–7690;
(h) Z. Hu, Q. Liu, S.L. Chou, S.X. Dou, Advances and challenges in metal sulfides/selenides for next-generation rechargeable sodium-ion batteries, Adv. Mater. 29 (2017) 1700606;
(i) X.Y. Yu, X.W. Lou, Mixed metal sulfides for electrochemical energy storage and conversion, Adv. Energy Mater. 8 (2018) 1701592;
(j) P. Geng, S. Zheng, H. Tang, R. Zhu, L. Zhang, S. Cao, H. Xue, H. Pang, Transition metal sulfides based on graphene for electrochemical energy storage, Adv. Energy Mater. 8 (2018) 1703259;
(k) J. Zhao, Y. Zhang, Y. Wang, H. Li, Y. Peng, The application of nanostructured transition metal sulfides as anodes for lithium ion batteries, J. Energy Chem. 27 (2018) 1536–1554;
(l) S. Dou, X. Wang, S. Wang, Rational design of transition metal-based materials for highly efficient electrocatalysis, Small Methods 3 (2019) 1800211.

[3] (a) Y. Du, Z. Yin, J. Zhu, X. Huang, X.J. Wu, Z. Zeng, Q. Yan, H. Zhang, A general method for the large-scale synthesis of uniform ultrathin metal sulphide nanocrystals, Nature Commun. 3 (2012) 1177;
(b) H. Zhang, B.R. Hyun, F.W. Wise, R.D. Robinson, A generic method for rational scalable synthesis of monodisperse metal sulfide nanocrystals, Nano Lett. 12 (2012) 5856–5860;
(c) D.Y. Chung, J.W. Han, D.H. Lim, J.H. Jo, S.J. Yoo, H. Lee, Y.E. Sung, Structure dependent active sites of NixSy as electrocatalysts for hydrogen evolution reaction, Nanoscale 7 (2015) 5157–5163;
(d) Y. Liu, H. Wang, L. Cheng, N. Han, F. Zhao, P. Li, C. Jin, Y. Li, TiS2 nanoplates: A high-rate and stable electrode material for sodium ion batteries, Nano Energy 20 (2016) 168–175.

[4] (a) Z. Li, X. Yu, A. Gu, H. Tang, L. Wang, Z. Lou, Anion exchange strategy to synthesis of porous NiS hexagonal nanoplates for supercapacitors, Nanotechnology 28 (2017) 065406;
(b) A.M. Patil, A.C. Lokhande, P.A. Shinde, J.H. Kim, C.D. Lokhande, Vertically aligned NiS nano-flakes derived from hydrothermally prepared Ni(OH)2 for high performance supercapacitor, J. Energy Chem. 27 (2018) 791–800.

[5] G. Rahman, S.Y. Chae, O.S. Joo, Efficient hydrogen evolution performance of phase-pure NiS electrocatalysts grown on fluorine-doped tin oxide-coated glass by facile chemical bath deposition, Int. J. Hydrogen Energy 43 (2018) 13022–13031.

[6] (a) X.Y. Yu, L. Yu, H.B. Wu, X.W. Lou, Formation of nickel sulfide nanoframes from metal-organic frameworks with enhanced pseudocapacitive and electrocatalytic properties, Angew. Chem. Int. Ed. 54 (2015) 5331–5335;
(b) C. Wei, C. Cheng, J. Zhao, Y. Wang, Y. Cheng, Y. Xu, W. Du, H. Pang, NiS hollow spheres for high-performance supercapacitors and non-enzymatic glucose sensors, Chem. Asian J. 10 (2015) 679–686;
(c) N. Jiang, Q. Tang, M. Sheng, B. You, D. Jiang, Y. Sun, Nickel sulfides for electrocatalytic hydrogen evolution under alkaline conditions: a case study of crystalline NiS, NiS2, and Ni3S2 nanoparticles, Catal. Sci. Technol. 6 (2016) 1077–1084;
(d) Y. Zhang, J. Xu, Y. Zhang, X. Hu, 3D NiS dendritic arrays on nickel foam as binder-free electrodes for supercapacitors, J. Mater. Sci.-Mater. Electron. 27 (2016) 8599–8605;
(e) P. Zhang, B.Y. Guan, L. Yu, X.W. Lou, Formation of double-shelled zinc-cobalt sulfide dodecahedral cages from bimetallic zeolitic imidazolate frameworks for hybrid supercapacitors, Angew. Chem. Int. Ed. 56 (2017) 7141–7145;
(f) B. Guan, Y. Li, B. Yin, K. Liu, D. Wang, H. Zhang, C. Cheng, Synthesis of hierarchical NiS microflowers for high performance asymmetric supercapacitor, Chem. Eng. J. 308 (2017) 1165–1173;
(g) X. Ma, L. Zhang, G. Xu, C. Zhang, H. Song, Y. He, C. Zhang, D. Jia, Facile synthesis of NiS hierarchical hollow cubes via Ni formate frameworks for high performance supercapacitors, Chem. Eng. J. 320 (2017) 22–28;
(h) N. Du, W. Zheng, X. Li, G. He, L. Wang, J. Shi, Nanosheet-assembled NiS hollow structures with double shells and controlled shapes for high-performance supercapacitors, Chem. Eng. J. 323 (2017) 415–424;
(i) J. Zhao, B. Guan, B. Hu, Z. Xu, D. Wang, H. Zhang, Vulcanizing time controlled synthesis of NiS microflowers and its application in asymmetric supercapacitors, Electrochim. Acta 230 (2017) 428–437;
(j) Y. Xu, W. Du, L. Du, W. Zhu, W. Guo, J. Chang, B. Zhang, D. Deng, Monocrystalline NiS nanowire arrays supported by Ni foam as binder-free electrodes with outstanding performances, RSC Adv. 7 (2017) 22553–22557;
(k) X. Xiao, D. Huang, Y. Fu, M. Wen, X. Jiang, X. Lv, M. Li, L. Gao, S. Liu, M. Wang, C. Zhao, Y. Shen, Engineering NiS/Ni2P heterostructures for efficient electrocatalytic water splitting, ACS Appl. Mater. Interfaces 10 (2018) 4689–4696;
(l) Z. Ma, Q. Zhao, J. Li, B. Tang, Z. Zhang, X. Wang, Three-dimensional well-mixed/highly-densed NiS-CoS nanorod arrays: An efficient and stable bifunctional

electrocatalyst for hydrogen and oxygen evolution reactions, Electrochim. Acta 260 (2018) 82–91;
(m) N. Parveen, S.A. Ansari, S.G. Ansari, H. Fouad, N.M.A. El-Salam, M.H. Cho, Solid-state symmetrical supercapacitor based on hierarchical flower-like nickel sulfide with shape-controlled morphological evolution, Electrochim. Acta 268 (2018) 82–93;
(n) S. Nandhini, A.J.C. Mary, G. Muralidharan, Facile microwave-hydrothermal synthesis of NiS nanostructures for supercapacitor applications, Appl. Surf. Sci. 449 (2018) 485–491;
(o) X. Shang, K.L. Yan, Y. Rao, B. Dong, J.Q. Chi, Y.R. Liu, X. Li, Y.M. Chai, C.G. Liu, In-situ cathodic activation of V-incorporated NixSy nanowires for enhanced hydrogen evolution, Nanoscale 9 (2017) 12353–12363;
(p) B. Dong, K.L. Yan, Z.Z. Liu, J.Q. Chi, W.K. Gao, J.H. Lin, F.N. Dai, Y.M. Chai, C.G. Liu, Urchin-like nanorods of binary NiCoS supported on nickel foam for electrocatalytic overall water splitting, J. Electrochem. Soc. 165 (2018) H102–H108.

[7] (a) W. Zhu, X. Yue, W. Zhang, S. Yu, Y. Zhang, J. Wang, J. Wang, Nickel sulfide microsphere film on Ni foam as an efficient bifunctional electrocatalyst for overall water splitting, Chem. Commun. 52 (2016) 1486–1489;
(b) Z. Liu, Y. Wang, R. Chen, C. Chen, H. Yang, J. Ma, Y. Li, S. Wang, Quaternary bimetallic phosphosulphide nanosheets derived from prussian blue analogues: Origin of the ultra-high activity for oxygen evolution, J. Power Sources 403 (2018) 90–96.

[8] (a) H. Pang, C. Wei, X. Li, G. Li, Y. Ma, S. Li, J. Chen, J. Zhang, Microwave-assisted synthesis of NiS2 nanostructures for supercapacitors and cocatalytic enhancing photocatalytic H2 production, Sci. Rep. 4 (2014) 3577;
(b) L. Peng, X. Ji, H. Wan, Y. Ruan, K. Xu, C. Chen, L. Miao, J. Jiang, Nickel sulfide nanoparticles synthesized by microwave-assisted method as promising supercapacitor electrodes: an experimental and computational study, Electrochim. Acta 182 (2015) 361–367;
(c) R. Thangavel, A.S. Pandian, H.V. Ramasamy, Y.S. Lee, Rapidly synthesized, few-layered pseudocapacitive SnS2 anode for high-power sodium ion batteries, ACS Appl. Mater. Interfaces 9 (2017) 40187–40196.

[9] N.P. Dasgupta, X. Meng, J.W. Elam, A.B.F. Martinson, Atomic layer deposition of metal sulfide materials, Acc. Chem. Res. 48 (2015) 341–348.

[10] S.H. Choi, Y.C. Kang, Aerosol-assisted rapid synthesis of SnS-C composite microspheres as anode material for Na-ion batteries, Nano Res. 8 (2015) 1595–1603.

[11] (a) H. Ruan, Y. Li, H. Qiu, M. Wei, Synthesis of porous NiS thin films on Ni foam substrate via an electrodeposition route and its application in lithium-ion batteries, J. Alloy. Compd. 588 (2014) 357–360;
(b) G. Kalaiyarasan, K. Aswathi, J. Joseph, Formation of nanoporous NiS films from electrochemically modified GC surface with nickel hexacyanoferrate film and its performance for the hydrogen evolution reaction, Int. J. Hydrogen Energy 42 (2017) 22866–22876;
(c) V.C. Tran, S. Sahoo, J.J. Shim, Room-temperature synthesis of NiS hollow spheres on nickel foam for high-performance supercapacitor electrodes, Mater. Lett. 210 (2018) 105–108;
(d) X. Shang, J.F. Qin, J.H. Lin, B. Dong, J.Q. Chi, Z.Z. Liu, L. Wang, Y.M. Chai, C.G. Liu, Tuning the morphology and Fe/Ni ratio of a bimetallic Fe-Ni-S film supported on nickel foam for optimized electrolytic water splitting, J. Colloid Interf. Sci. 523 (2018) 121–132.

[12] M. Kristl, B. Dojer, S. Gyergyek, J. Kristl, Synthesis of nickel and cobalt sulfide nanoparticles using a low cost sonochemical method, Heliyon 3 (2017) e00273.

[13] (a) A.M. Darwish, W.H. Eisa, A.A. Shabaka, M.H. Talaat, Synthesis of nano-cadmium sulfide by pulsed laser ablation in liquid environment, Spectr. Lett. 48 (2015) 638–645;
(b) Y. Zhou, H. Liu, J. Yang, J. Mao, C.K. Dong, T. Ling, X.W. Du, Scalable synthesis of cubic Cu1.4S nanoparticles with long-term stability by laser ablation of salt powder, Chem. Commun. 52 (2016) 811–814;
(c) K.Y. Niu, L. Fang, R. Ye, D. Nordlund, M.M. Doeff, F. Lin, H. Zheng, Tailoring transition-metal hydroxides and oxides by photon-induced reactions, Angew. Chem. Int. Ed. 55 (2016) 14272–14276;
(d) A.M. Darwish, W.H. Eisa, A.A. Shabaka, M.H. Talaat, Investigation of factors affecting the synthesis of nano-cadmium sulfide by pulsed laser ablation in liquid environment, Spectro. Acta Pt. A-Molec. Biomolec. Spectr. 153 (2016) 315–320;
(e) G.G. Guillén, M.I.M. Palma, B. Krishnan, D.A. Avellaneda, S. Shaji, Tin sulfide nanoparticles by pulsed laser ablation in liquid, J. Mater. Sci.-Mater. Electron. 27 (2016) 6859–6871;
(f) K. Savva, B. Višić, R. Popovitz-Biro, E. Stratakis, R. Tenne, Short pulse laser synthesis of transition-metal dichalcogenide nanostructures under ambient conditions, ACS, Omega 2 (2017) 2649–2656;
(g) G.G. Guillén, V.A.Z. Ibarra, M.I.M. Palma, B. Krishnan, D.A. Avellaneda, S. Shaji, Effects of liquid medium and ablation wavelength on the properties of cadmium sulfide nanoparticles formed by pulsed-laser ablation, ChemPhysChem 18 (2017) 1035–1046;
(h) M. Khademian, M. Zandi, M. Amirhoseiny, D. Dorranian, Synthesis of CuS nanoparticles by laser ablation method in DMSO media, J. Clust. Sci. 28 (2017) 2753–2764.

[14] (a) J. Yan, G. Lui, R. Tjandra, X. Wang, L. Rasenthiram, A. Yu, α-NiS grown on reduced graphene oxide and single-wall carbon nanotubes as electrode materials for high-power supercapacitors, RSC Adv. 5 (2015) 27940–27945;
(b) L. Shen, L. Du, S. Tan, Z. Zang, C. Zhao, W. Mai, Flexible electrochromic supercapacitor hybrid electrodes based on tungsten oxide films and silver nanowires, Chem. Commun. 52 (2016) 6296–6299.

[15] A.V. Naumkin, A. Kraut-Vass, S.W. Gaarenstroom, C.J. Powell, NIST Standard Reference Database 20, Version 4.1 (Web Version), 2018, http:/srdata.nist.gov/xps/.

[16] (a) L. Ren, Z. Jin, W. Wang, H. Liu, J. Lai, J. Yang, Z. Hong, Preparation and characterization of SnS nanocrystals by a triethanolamine-assisted diethylene glycol solution synthesis, Appl. Surf. Sci. 258 (2011) 1353–1358;
(b) M. Du, X. Yin, H. Gong, Effects of triethanolamine on the morphology and phase of chemically deposited tin sulfide, Mater. Lett. 22 (2015) 40–44.

[17] C.C.L. McCrory, S. Jung, I.M. Ferrer, S.M. Chatman, J.C. Peters, T.F. Jaramillo, Benchmarking hydrogen evolving reaction and oxygen evolving reaction electrocatalysts for solar water splitting devices, J. Am. Chem. Soc. 137 (2015) 4347–4357.

[18] C.C.L. McCrory, S. Jung, J.C. Peters, T.F. Jaramillo, Benchmarking heterogeneous electrocatalysts for the oxygen evolution reaction, J. Am. Chem. Soc. 135 (2015) 16977–16987.

[19] A. Sukeri, L.P.H. Saravia, M. Bertotti, A facile electrochemical approach to fabricate a nanoporous gold film electrode and its electrocatalytic activity towards dissolved oxygen reduction, PCCP 17 (2015) 28510–28514.

[20] X. Wang, R. Liu, Y. Zhang, L. Zeng, A. Liu, Hierarchical Ni_3S_2-NiOOH hetero-nanocomposite grown on nickel foam as a noble-metal-free electrocatalyst for hydrogen evolution reaction in alkaline electrolyte, Appl. Surf. Sci. 456 (2018) 164–173.

[21] C. Johnston, P.R. Graves, In situ Raman spectroscopy study of the nickel oxyhydroxide electrode (NOE) system, Appl. Spectrosc. 44 (1990) 105–115.

[22] C. Yuan, X. Zhang, L. Su, B. Gao, L. Shen, Facile synthesis and self-assembly of hierarchical porous NiO nano/micro spherical superstructures for high performance supercapacitors, J. Mater. Chem. 19 (2009) 5772–5777.

[23] (a) J. Yang, X. Duan, Q. Qin, W. Zheng, Solvothermal synthesis of hierarchical flower-like β-NiS with excellent electrochemical performance for supercapacitors, J. Mater. Chem. A 1 (2013) 7880–7884;
(b) Z. Li, J. Han, L. Fan, R. Guo, Template-free synthesis of Ni7S6 hollow spheres with mesoporous shells for high performance supercapacitors, CrystEngComm 17 (2015) 1952–1958;
(c) Z. Li, J. Han, L. Fan, R. Guo, In-situ controllable growth of α-Ni(OH)2 with different morphologies on reduced graphene oxide sheets and capacitive performance for supercapacitors, Colloid Polym. Sci. 294 (2016) 681–689.